Chemical Engineering Journal 433 (2022) 133260

Contents lists available at ScienceDirect

Chemical Engineering Journal

journal homepage: www.elsevier.com/locate/cej

Multiple H-bonding chain extender-based polyurethane: Ultrastiffness, hot-melt adhesion, and 3D printing finger orthosis

Meng Xiao, Yuan Yao, Chuanchuan Fan, Ziyang Xu, Yang Liu, Bo Liu, Jia Li, Xiaoping Zhang, Xin Jin, Jumin Yang, Jianhai Yang *, Wenguang Liu *

School of Material Science and Engineering, Tianjin Key Laboratory of Composite and Functional Materials, Tianjin University, Tianjin 300350, China

ARTICLE INFO

Keywords:
Polyurethane
Ultrastiff
3D printing
Finger orthosis

ABSTRACT

Mallet finger is a common athletic injury, and the current treatment involves fixing the injured finger by a splint or orthosis. 3D printing technology offers an innovative way to customize patient-specific finger orthosis that fits the individual anthropometrics. However, the existing printed materials cannot combine the high stiffness and toughness to construct an ideal finger orthosis. Herein, we report a new chain extender carrying one amide and one urea group in the side chain, and utilize it to extend polyurethane prepolymer to fabricate a highly stiff and tough thermoplastic polyurethane (TPU). Strong and mobile H-bonds in the side chain promote the formation of multiphase-separated structure in the TPU network, thus endowing this TPU with high Young's modulus (213.0 $\pm$ 3.7 MPa) and high toughness (47.8 $\pm$ 1.9 MJ m^{-3}). Due to the dynamic H-bonds in the polymer network, this TPU exhibits an excellent 3D printing ability, and can be used to print finger orthosis by fused deposition modeling technology at an elevated temperature. The printed finger orthosis can be attached with a wireless pulse oximeter by virtue of TPU adhesiveness, thus monitoring vital physiological signals on the injured index finger that can be well fixed by the stiff orthosis.

1. Introduction

Humans create our beautiful world with their own hands, which are amazingly dextrous appendages capable of performing countless actions and doing all kinds of things; while the hand functions require the coordinated action of fingers. Because of overuse of fingers each day, they are prone to injury, frequently causing mallet finger (MF), also known as "baseball finger" or "drop finger", which is defined as a permanent deformity in the finger that cannot straighten on its own [1]. The reason for the occurrence of mallet finger is that the extensor tendon responsible for straightening the finger is hurt by a severe impact, resulting in the loss of the extensor mechanism at the distal interphalangeal (DIP) joint [2]. The injury significantly affects the working performance and capability to preform daily activities. The current treatment involves fixing the injured finger by a splint made of a thermoplastic or plaster material to maintain full extension or slight hyperextension at the DIP joint [3]. However, the plaster is too heavy and cannot be detected by X-ray. In addition, removal of plaster tends to cause secondary pain when conducting a computed tomography (CT) examination. The thermoplastic splint is used commonly. However, its fixation effect is dependent on the skill of a surgeon since the conventional splints made by cast molding are not suited for all patients' finger structure; moreover, post-processing can produce extra waste [4].

Recently, 3D printing technology has brought about an innovative way to customize tissue engineering scaffolds, organoid and orthotic for personized therapy [5,6]. The main benefits of the 3D printed orthosis include three points: it can be customized according to the patient anthropometrics, thus fitting the physiological curve; it saves time and raw material, and can be manufactured on a large scale; it enables fabrication of complex architecture without losing the comfortability.

A variety of polymer materials, such as poly-lactic-acid (PLA) [7], acrylonitrile-butadiene styrene (ABS) [8] and thermoplastic polyurethane (TPU) [9], can be used to construct orthotic scaffold via the fused deposition modeling (FDM) method, and the printed orthotic devices can match or surpass the function of current thermoplastic splints. The material for finger orthosis is required to possess a high stiffness and an appropriate elastic resilience to fix the finger joints. TPUs are linear multiblock copolymers with tunable viscosity under heating condition and can be used as 3D printing inks. However, the conventional TPUs suffer from the well-known trade-off between toughness and stiffness,

* Corresponding authors.
E-mail addresses: jianhaiyang@tju.edu.cn (J. Yang), wgliu@tju.edu.cn (W. Liu).

https://doi.org/10.1016/j.cej.2021.133260
Received 20 June 2021; Received in revised form 15 September 2021; Accepted 26 October 2021
Available online 1 November 2021

which makes them unsuitable for constructing finger orthosis [10]. Recently, highly stiff and tough thermoplastic polyurethanes reinforced by dual crosslinks [11], sliding crosslinks [12], and multiple H-bonds [13–15] have been reported. Those TPUs can maintain 2.0–105.9 MPa Young's modulus; nonetheless, few of them have been exploited as printable inks of orthopedic scaffolds.

Lately, our group reported a supramolecular polyurethane prepared from PU prepolymer and multiple hydrogen bonding chain extender *N, N*-bis(2-hydroxyethyl)-3-amino propionyl glycinamide (OH-NAGA-OH) [13]. The side-chain combined with backbone hydrogen bonds contributed to high stiffness (up to 28.18 MPa) and toughness (up to 11.4 MJ m^{-3}) and mobile side-chain H-bonds afforded room temperature autonomous healability. However, the modulus of this polyurethane cannot meet the requirement for constructing finger orthosis. Recently, our group developed a new supramolecular poly(N-acryloyl semicarbazide) (PNASC) whose side chain contained an additional hydrogen bonding donor, *NH* compared to poly(N-acryloyl glycinamide) (PNAGA). Introduction of this extra *NH* in side chain considerably enhanced H-bonding crosslinking density, eventually led to formation of an ultrastiff hydrogel with the highest Young's modulus of 100.3 MPa, and toughness of 20.35 MJ m^{-3} [16]. Inspired by the strengthening principle of side chain H-bonds of NAGA-based diol in preparing supramolecular PU, we propose to design a NASC-based diol chain extender, which will react with a PU prepolymer to synthesize an upgraded supramolecular PU elastomer (PU-NASC) (Fig. 1a). We hypothesize that much denser H-bonding crosslinks from NASC-based diol can enhance tremendously the stiffness and toughness of the resultant PU elastomer (Fig. 1b). We also anticipate that dynamic H-bonding interactions will afford reversible thermoplasticity of the PU, which can be further developed as a printable ink. And the PU ink is printed to a finger orthosis via melt extrusion. We can imagine that the printed supramolecular PU elastomer finger orthosis is rigid enough to fix the injured index finger (Fig. 1c). The printed tailor-made microholes will allow for breathability without sacrificing the structure stability [17]. Furthermore, in light of thermoplastic behavior, this PU elastomer can be used as hot-melt adhesive with a high adhesive and cohesive strength. We will attach a commercial sensor to the surface of the PU finger orthosis by its own high adhesion force. The bound sensor can measure the vital physiological signals, such as blood oxygen saturation, heart rate, blood pressure and pulse wave, and the signals are transmitted to a smartphone via Bluetooth, realizing real-time monitoring of health status [18,19].

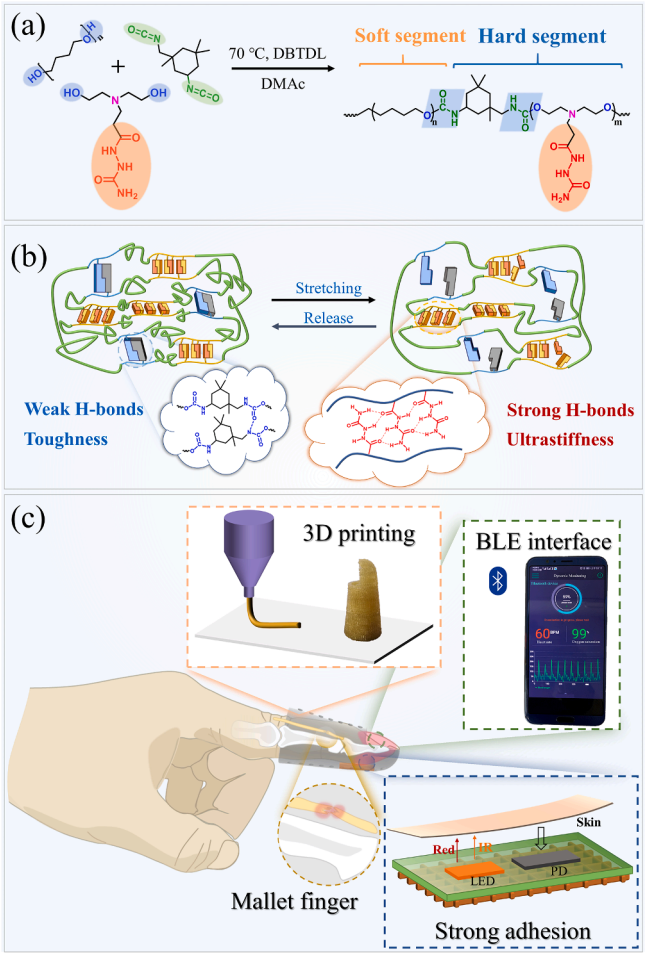

Fig. 1. Schematic illustration of synthesis of NASC diol extended polyurethane with ultrastiffness and toughness. a) Synthesis route of PU-NASC. b) Stiffening and toughening mechanism of PU-NASC. c) 3D printing of finger orthosis for treating mallet finger and monitoring vital physiological signs by the attached sensor.

2. Material and methods

2.1. Materials

Semicarbazide hydrochloride (98%), acryloyl chloride (98%), N,N-diethanolamine (DEA) (99%) were obtained by Tokyo Chemical Industry Co. Ltd (Shanghai, China). Polytetramethylene ether glycol (PTMG, Mn = 1000 g mol^{-1}), isophorone diisocyanate (IPDI, 99%), dibutyltin dilaurate (DBTDL, 97%) were purchased from Sigma-Aldrich (Shanghai, China). NASC was synthesized according to the previous work [13,16]. All other chemicals and solvents were analytical reagents and used as received without further purification.

2.2. Synthesis of N,N-bis(2-hydroxyethyl)-3-amino propionyl semicarbazide (NASC diol)

NASC (10.0 g, 77 mmol) was dissolved in 40 ml hot water, followed by adding dropwise 10 ml aqueous solution of DEA (5.09 g, 48 mmol). The mixture was stirred at 40 °C for 48 h until the reaction was completed. Then the solvent was removed by rotary evaporation. The crude product was dissolved in methanol to remove the excess NASC monomer, and then the solution was evaporated and washed by acetone several times until the neutral pH was reached. The resultant product NASC diol was dried in a vacuum oven.

2.3. Preparation of polyurethane

1.5 g PTMG (1.50 mmol) was heated at 120 °C in a 100 ml three-necked glass flask under vacuum and mechanically stirred for 2 h to remove water. Then the melted PTMG was cooled down to 70 °C, followed by addition of a certain amount of IPDI and one drop of catalyst DBTDL under a nitrogen atmosphere. After that the mixture was further stirred for 3 h at 70 °C. Finally, the prescribed amount of NASC-diol in dimethylacetamide (DMAc) was added into the PU prepolymer and stirred at room temperature for 18 h to complete the reaction. The viscous PU polymer solution was poured into customized polyethylene mold and dried at 70 °C for 48 h to remove DMAc under vacuum, and a colorless yet transparent PU-NASC film was obtained. We also prepared PU-NAGA film as control group following our previous work [13].

2.4. Mechanical testing

The PU-NASC films were cut into the dumbbell specimen with a size of 50 mm length × 4 mm width × 1 mm height by the punching machine. The tensile test of the specimen was performed on a Legend 2344 electromechanical dynamometer (Instron, USA) at a strain speed of 50 mm min^{-1}. The Young's modulus was calculated from the initial slope linear stage of the stress–strain curves, and the toughness was calculated

by integrating the area under the stress–strain curve. The cyclic tensile tests were performed for 10 times under a tensile speed of 50 mm min^{-1}.

2.5. Determination of fracture energy

According to the Rivlin and Thomas method [20], two different samples, the notched one and the unnotched one were used to measure the fracture energy E_f. The rectangular shaped specimens (8 mm × 30 mm × 1 mm) were prepared, and then an initial notch of 1 mm was cut in the middle by a razor blade. The specimen was clamped on the two sides, and the distance between the two clamps was fixed at 10 mm. Then the specimen was pulled to fracture at 50 mm min^{-1}. The force–displacement curves of the samples were recorded, and the fracture energy was calculated using the following equation:

$$E_f = \frac{U(L_c)}{a_0 \times b_0} \quad (1)$$

Where a_0 and b_0 were the thickness and width of the sample, respectively; $U(L_c)$ was the work done by the unnotched sample at critical stretching distance L_c. In this experiment, L_c was defined as the transition point from yielding stage to breaking stage.

2.6. Lap-shear test

PU-NASC and commercial PU adhesives were melted and reshaped into a film, respectively, and then placed between two identical substrates. The two substrates were pressed gently and held by two paper clips, and cured for 20 min at 100 °C. After cooling down to room temperature, the lap-shear testing was carried out on a Legend 2344 electromechanical dynamometer at a strain rate of 50 mm min^{-1}. The lap-shear strength was calculated according to the method published [21,22]. Each measurement was repeated at least three times.

2.7. Characterizations

The chemical structures of NASC diol and PU-NASC were characterized on a nuclear magnetic resonance spectrometer (NMR, AVANCE III, 400 MHz, Bruker) and an attenuated total reflection Fourier transform infrared spectrometer (ATR-FTIR, Nicolet 6700, Thermo Scientific). Variable temperature ^{1}H NMR spectra were recorded on an NMR spectrometer (ECZ600R, 600 MHz, JEOL) with a varied temperature from 30 to 100 °C to examine the thermal dissociation of H-bonds. The molecular weight and molecular weight distribution were evaluated on a Gel permeation chromatography (1260 Infnity II, Agilent). The transparency of PU-NASC films was evaluated on a UV–vis spectrophotometer (GENESYS 180UV, Thermo Scientific) with quick mode from 400 to 800 nm. The film thickness was 0.5 mm. The crystal phase of PU-NASC was analyzed via X-ray diffraction (XRD, D8 Advanced, Bruker) using Cu Kα radiation (λ = 0.154 nm) from 5° to 40° at a scanning rate of 4 min^{-1}. The surface topographies of PU-NASC films were measured on an atomic force microscope (AFM, CSPM5500A, Beijing Nano-Instruments) with the tapping mode. The cytotoxicity and live/dead assays of the PU-NASC polyurethane were conducted using the reported co-culture method [23].

2.8. Thermal analysis

The glass transition temperature (T_g) was measured on a differential scanning calorimetry (DSC, 200 F3, Netzsch, Germany) over a temperature range from − 50 °C to 180 °C at a heating rate of 5 °C min^{-1} under a nitrogen atmosphere. The heating process was conducted twice to eliminate the heat history and the influence of other factors. $T_{0.5}$, the endothermic shift temperature at half-height from the DSC curves, is recommended by ASTME 1356-91 to determine T_g [24]. Thermo gravimetric analysis (TGA) was conducted on a simultaneous thermal analyzer instrument (STA449F3, Netzsch, Germany) with a heating rate of 5 °C min^{-1} from 30 to 800 °C under a nitrogen atmosphere. The sample was kept dry before testing.

2.9. Small-angle X-ray scattering

The small angle X-ray scattering studies were performed using a NanoSTAR system (Bruker, Germany). The PU-NASC film was cut into a rectangular sample (10 mm × 5 mm × 1 mm) and fixed on the clear aperture of the sample stage. The X-ray wavelength was set as 0.154 nm, the distance between detector and sample was set as 1050 nm, and the effective scattering vector range q was from 0.02 to 0.2 nm^{-1} ($q = \frac{4\pi\sin\theta}{\lambda}$, where 2θ is the scattering angle and λ is the wavelength). The 1D scattering intensity distribution was obtained by integrating the 2D scattering pattern, and the final result was analyzed.

2.10. Rheological measurement

Rheological measurements were conducted on a rheometer (MCR-302, Anton-Paar, Austria) using a 25 mm-diameter parallel plate. The disk was pressed with a force of 5 N to avoid slippage. Temperature sweeps were performed at a frequency of 1 Hz over a temperature range from 80 to 120 °C. Frequency sweeps were conducted at a strain amplitude of 0.1% in a frequency range from 0.001 to 100 rad s^{-1}.

2.11. Dynamic mechanical behavior

The storage modulus and loss modulus of PU-NASC films over a temperature range from −80 to 60 °C were measured on a dynamic mechanical analyzer (Q800, TA, USA). The samples were stretched at a dynamic strain of 0.1% and a constant frequency of 1 Hz with a heating rate of 5 °C min^{-1}.

2.12. Design of the 3D printed orthosis

The model of patient-specific orthosis was first designed using the CAD/CAM software by measuring several parameters of a patient's healthy index finger (Fig. S18, Supporting Information). The finger orthosis was designed with an open ventilation section above the fingernail to allow airflow and reduce sweating when it was worn. The top section of the orthosis extended to the proximal interphalangeal joint. This allowed for the patient's flexion of the finger without influencing recovery.

2.13. 3D printing of the PU-NASC constructs

PU-NASC constructs were fabricated on a Bio-Architect® Sparrow 3D printer (Regenovo Biotechnology Co. Ltd, Hangzhou, China) by a screw extrusion method. The platform was heated to 45 °C before the printing process. The extraction nozzle diameter, printing speed, and extraction speed was set as 0.3 mm, 3 mm min^{-1}, and 0.5 mm min^{-1}, respectively; the raster width was fixed as 0.6 mm. The PU-NASC fragments were loaded into the stainless-steel syringe and were extruded through a nozzle, whose temperature was set as 140 °C to allow a fluent printing process. Finally, the printed constructs were removed easily from the printing plate.

2.14. Finite element analysis of 3D printed finger orthosis

The finite element analysis (FEA, ANSYS 2019 R2, ANSYS, Inc) was conducted to analyze the distribution of deflection and stress of 3D printed finger orthosis under realistic conditions. The Young's modulus of the printed subject was set as 100 MPa and Poisson's ratio set as 0.47. Two simulation situations were conducted. An external load of 10 N was applied on 1 cm^2 area of the upper surface of the orthosis, simulating the

compression exerted on the orthosis. Another simulation was conducted in a static structure module to evaluate required compressive strength required for maintaining full extension of the mallet finger.

3. Results and discussion

3.1. Preparation and characterization of PU-NASC

Herein, we first synthesized a novel T-shaped chain extender OH-NASC-OH (NASC diol) by Michael addition reaction of NASC monomer with *N,N*-diethanolamine, whose side chain containing an amide group and adjacent urea group. The chemical structure of NASC diol was verified by ^{1}H NMR spectrum (Fig. S1). According to our previous reported method [13], the desired supramolecular polyurethane was synthesized by prepolymerization reaction of polytetramethylene ether glycol (PTMG) and isophorone diisocyanate (IPDI), and then the PU prepolymer was chain-extended by NASC diol to form the final PU-NASC, which was named as PU-NASC-x (x denoted the molar ratio of NASC diol to PTMG). The molecular structure of PU-NASC-x were confirmed by the ^{1}H NMR spectrum and attenuated total reflection Fourier transform infrared (ATR-FTIR) spectra (Figs. S2–S3). The absence of stretching vibration bond of –NCO at 2260–2280 cm^{-1} indicates the complete reaction of IPDI, and the ATR-FTIR spectra show the characteristic band of PU-NASC-x: the stretching vibration peak of –NH_2 bond at 3300 cm^{-1}, and the bending vibration peak of –NH- at 1537 cm^{-1}; the stretching vibration peak of free C=O bond at 1690 cm^{-1}, and the stretching vibration peak of hydrogen-bonded C=O bond at 1660 cm^{-1} [26,27].

The viscoelastic behavior of PU-NASC was characterized by dynamic mechanical analysis (Fig. 2a). As temperature was increased above 60 ℃, both the storage modulus (G') and loss modulus (G'') of PU-NASC dropped sharply, and the intersections occurred gradually, implying that increased flexibility of polymer chains, which may be originated from the dissociation of most intermolecular H-bonds at high temperature. Next, the dissociation kinetics of the H-bonds between C=O and N–H in PU-NASC at different temperature were further studied by variable temperature (VT) ^{1}H NMR spectroscopy and ATR-FTIR spectroscopy (Fig. 2b and Fig. S4). As shown in Fig. 1b, the peaks of those NH protons shifted to high field and became wider with an elevated temperature [28]. Moreover, the wavenumber of C=O stretching signal exhibits a blue shift in ATR-FTIR (Fig. S4) spectra with the increase of temperature from 30 to 120 °C [29]. All these shifts indicated the dissociation of H-bonds between N–H and C=O species as the temperature increased, suggesting the existence of a large amount of intermolecular and intramolecular H-bonds in the PU-NASC. The PU-NASC film could be dissolved in dimethylacetamide (DMAc), and then a recycled PU-NASC film could be obtained via the casting method (Fig. 2c), and exhibited an excellent recoverable mechanical property, which was

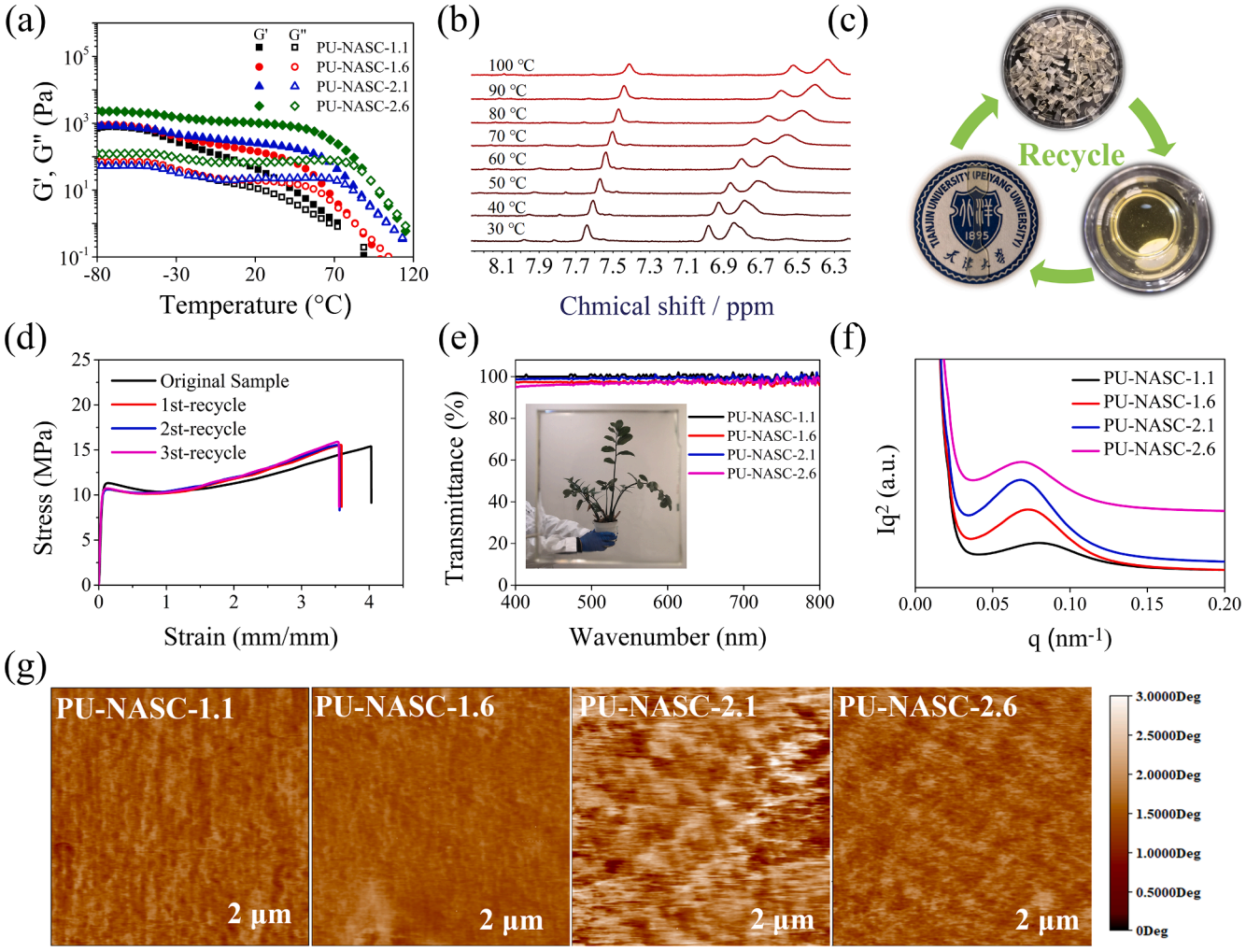

Fig. 2. Characterization of PU-NASC-x elastomers. a) Variation in viscoelastic behavior of PU-NASC-x as a function of temperature. b) VT ^{1}H NMR spectra of PU-NASC-2.1 with varied temperatures. c) Solvent recycle process of PU-NASC-2.1 films. d) Typical stress–strain curves of the recycled PU-NASC-2.1 film under the first, second, and third recycle process. e) Transmittance of PU-NASC-x films to visible light in the range from 400 to 800 nm. Inset image shows the excellent transparency of PU-NASC-2.1 film. f) Iq^2–q profiles of PU-NASC-x. g) AFM images of PU-NASC-x.

confirmed by the stress–strain curves (Fig. 2d). The molecular weight of PU-NASC-x with different NASC-diol content was in the range from 17,300 to 25,300 g/mol (Table S1). All these results indicated the successful synthesis of PU-NASC polyurethane, and its multiple dynamic H-bonding crosslinked structure.

The morphological structure of the PU-NASC was characterized using wide-angle X-ray diffraction (WAXD) (Fig. S5). The WAXD patterns of PU-NASC exhibited a broad diffraction peak centered at $2\theta = 19.5°$. Moreover, there was no melting endothermic peak of crystalline polyurethane either in the DSC curves of PU-NASC over a temperature range from −50 to 100 °C (Fig. S6). All these results suggested amorphous nature of PU-NASC [30]. Therefore, the PU-NASC films exhibited a high transmittance over 95% in a visible wavelength range from 400 to 800 nm (Fig. 2e). The glass transition temperatures of the PU-NASC were increased from 47 to 56 °C with the increment of NASC diol content (Table S1), which were all much higher than those of the reported PU-NAGA [13], indicating much stronger multiple H-bonds formed in the PU-NASC due to the replacement of CH_2 with NH. Previous reports revealed that aggregations of multiple H-bonds could lead to the formation of multiphase separation structure [31]. Next, we used small angle X-ray scattering (SAXS) and atomic force microscope (AFM) to study the microphase separation of the PU-NASC. As shown in Iq^2-q curve (Fig. 2f), the primary scattering peak shifted toward a lower q value, and the periodicity ($d = 2\pi/q^*$) of the phase-separated domains increased from 76.1 to 90.1 nm with the increase of NASC diol content (Fig. S7). These sizes are all much larger than those of PU-NAGA [13], implying that PU-NASC owned much denser multiple H-bonds than PU-NAGA. In addition, the full width at half maximum of the scattering peaks was gradually narrowed with increasing NASC-diol content, indicating the boundaries of microphase structure became clearer. The scattering circles in the 2D-SAXS scattering patterns were also more clearly observed (inset image in Fig. S8), hinting the more H-bond clusters were formed in the hard segment of PU-NASC [32]. Moreover, in the AFM images the PU-NASC exhibited a microphase separation structure, where the darker part corresponded to the aggregations of the soft PTMG segments and the brighter part was assigned to the H-bonded aggregates of the hard segment (Fig. 2g). With the increase of NASC-diol content in the hard segment, the interface between dart region and bright region became clearer, further indicating the formation of microphase separation. It is noted that more evident microphase separation occurred in PU-NASC-2.1 than in PU-NASC-2.6. A probable reason is that much stronger H-bonding interactions in the PU-NASC-2.6 constricted the movement of the soft segment, thus inhibiting the formation of microphase-separated domains [33]. All these outcomes hinted that replacement of CH_2 in the side chain of NAGA diol with NH group could improve the interactions of multiple H-bonds and promote the formation of microphase structure, thus contributing to much higher stiffness, toughness and adhesive strength.

3.2. Mechanical properties of PU-NASC

In the following experiment, the mechanical properties of PU-NASC films with different molar ratios of NASC diol/PTMG were evaluated via tensile test. As shown in the stress–strain curve in Fig. 3a, all PU-NASC films exhibited an escalating initial stiffening region followed by a yielding region due to the presence of dynamic inter-chain H-bonds.

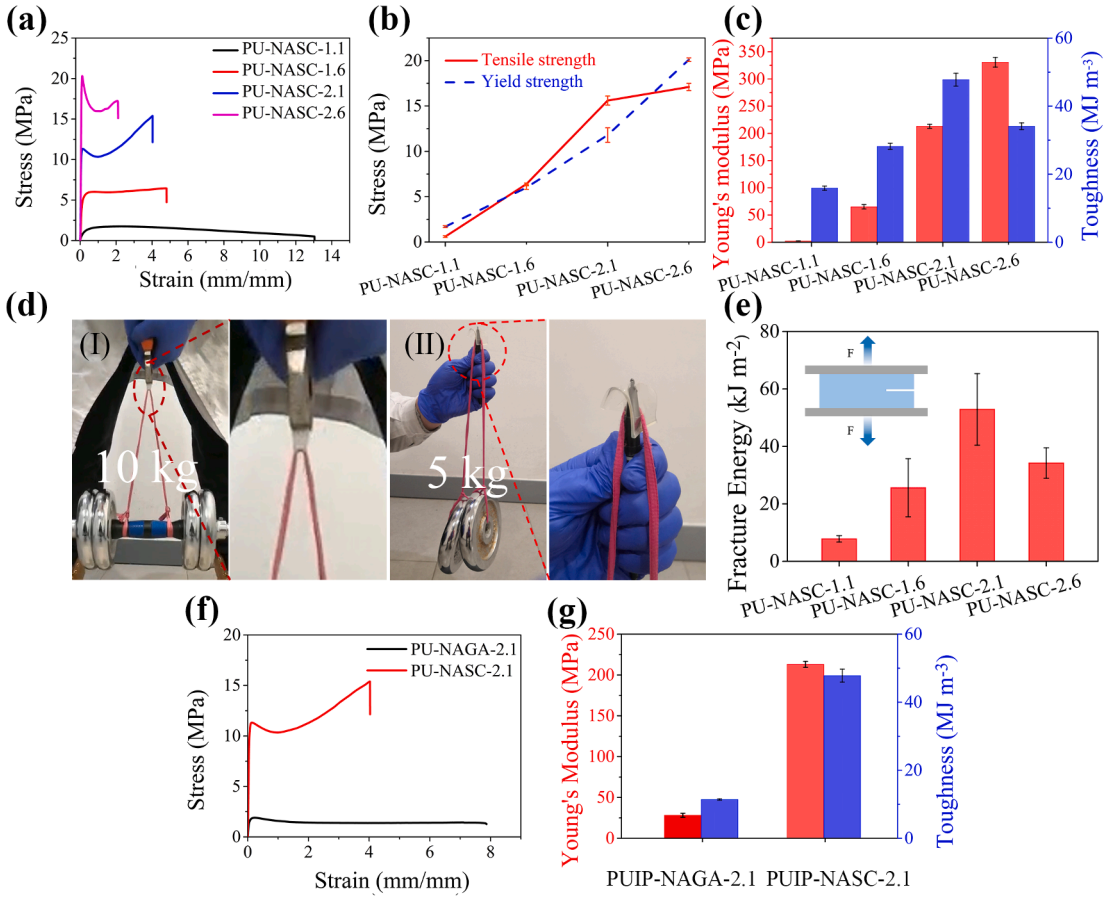

Fig. 3. Mechanical properties of PU-NASC-x. a) Typical stain-stress curves, and b) the corresponding tensile strength and yield strength, and c) Young's modulus and fracture toughness of PU-NASC-x. d) I) Photograph showing that the PU-NASC-2.1 film could withstand a 10 kg dumbbell with minor deformation, and II) Resistance of PU-NASC-2.1 film to the nib (diameter = 2 mm) puncture. e) Fracture energy of PU-NASC-x. f) Typical stain-stress curves and g) Young's modulus and toughness of PU-NASC-2.1 and PU-NAGA-2.1.

With the lowest H-bonds density, the PU-NASC-1.1 underwent a continuous deformation upon applying a strain, and displayed a tensile strength of 0.6 ± 0.1 MPa, Young's modulus of 2.4 ± 0.1 MPa, elongation at break of 1270 ± 90%. While with an increment of NASC diol content, the tensile strength and Young's modulus of PU-NASCs were significantly enhanced due to much denser H-bonding interactions. Specifically, the PU-NASC-2.6 gained a higher yield strength than the tensile strength owing to the restriction of the dense H-bonds to sufficient stretching of polymer chains (Fig. 3b). The PU-NASC-2.1 obtained a tensile strength of 15.6 ± 0.5 MPa, Young's modulus of 213.0 ± 3.7 MPa, and toughness of 47.8 ± 1.9 MJ m^{-3}, while corresponding values of PU-NASC-2.6 were 17.4 ± 0.4 MPa, 330.6 ± 8.9 MPa, and 34.1 ± 1.0 MJ m^{-3}, respectively (Fig. 3c). In comparison, the Young's modulus of PU-NASC-2.1 and PU-NASC-2.6 was respectively increased by 88, and 138 times compared to that of PU-NASC-1.1. Among these, the PU-NASC-2.6 exhibited a higher modulus and lower toughness than PU-NASC-2.1.

Interestingly, a rectangular PU-NASC-2.1 film (30 mm × 8 mm × 1 mm) could bear a weight of 10 kg dumbbell with only a slight deformation, and could lift a 5 kg dumbbell without occurrence of piercing when a nib served as the supporting point, indicating high stiffness and excellent fracture resistance. The fracture resistance of PU-NASC was further evaluated by a crack propagation experiment on single-edged notched sample (Fig. S9). The fracture energies of PU-NASC-1.1, PU-NASC-1.6, PU-NASC-2.1 were respectively 7.8 ± 1.1, 25.6 ± 10.1, 52.9 ± 12.4 kJ m^{-2}, which were increased with the increment of NAGA diol content. The outstanding performance of the PU-NASC-2.1 may be attributed to the synergistic balance of weak H-bonding interactions in the main chains and strong multiple side-chain H-bonding interactions in the side chains in the PU-NASC network. When stretched, the weak H-bonds broke first to dissipate energy, resulting in a high toughness, whereas the strong H-bonding crosslinks contributed to a high stiffness [34].

The effective energy dissipation of PU-NASC-2.1 was further evaluated by the cyclic loading–unloading test (Fig. S10). The PU-NASC-2.1 specimen could resist 10 continuous loading–unloading cycles without break at a strain of 300% and tensile speed of 50 mm min^{-1}. During the test, a large hysteresis and notable residual strain were only observed in the first cycle, and the hysteresis areas were gradually decreased to a steady region in the subsequent nine cycles, indicating a better elastic recovery [35]. In a word, the PU-NASC-2.1 demonstrated a high stiffness and excellent toughness due to the balance of energy dissipation between the strong H-bonds and weak H-bonds [36].

Compared with the chain extender NAGA diol, NASC diol could form much denser H-bonding interactions in the side chain, thus resulting in a considerable enhancement in the mechanical properties of the PUs. The tensile strength, Young' modulus and toughness of the PU-NASC-2.1 were respectively increased by 8.2, 7.6, and 4.2 times compared to those of PU-NAGA-2.1 (Fig. 3f-g). The PU-NASC-2.1 film was stiff enough to lift a 10 kg dumbbell with only minor deformation; while the PU-NAGA-2.1 was ruptured (Movie S1). The PU-NASC-2.1 polyurethane simultaneously exhibited a high modulus and toughness (Table S2), suggesting its suitability for printing finger orthosis.

3.3. Adhesion ability of PU-NASC

Taking account of the dissociation behavior of multiple H-bonds under high temperature, the thermoplastic property of PU-NASC-2.1 was further examined by the rheological temperature sweep test. As shown in Fig. 4a, a crossover point was observed between the storage modulus (G') and the loss modulus (G'') at 96.5 ℃, indicating the transition from hard elastic state to viscous flow state of the PU-NASC. When temperature was above 96.5 ℃, the PU-NASC exhibited a liquid-like behavior due to the dissociation of dynamic H-bonds.

Thus, the PU-NASC-2.1 with high bulk strength was used as hot-melt adhesive to glue different substrates including fiberglass board, epoxy resin, aluminum, and ceramics. Typically, two pieces of substrates were glued together with a PU-NASC-2.1 film in between, and clamped by clips, followed by promoting adhesion in an oven at 100 °C for 30 min, and cooling down to room temperature. Notably, the adhered aluminum sheets could withstand a 20 kg dumbbell without occurrence of stretching deformation (Fig. 4b and Movie S2). The lap-shear adhesion

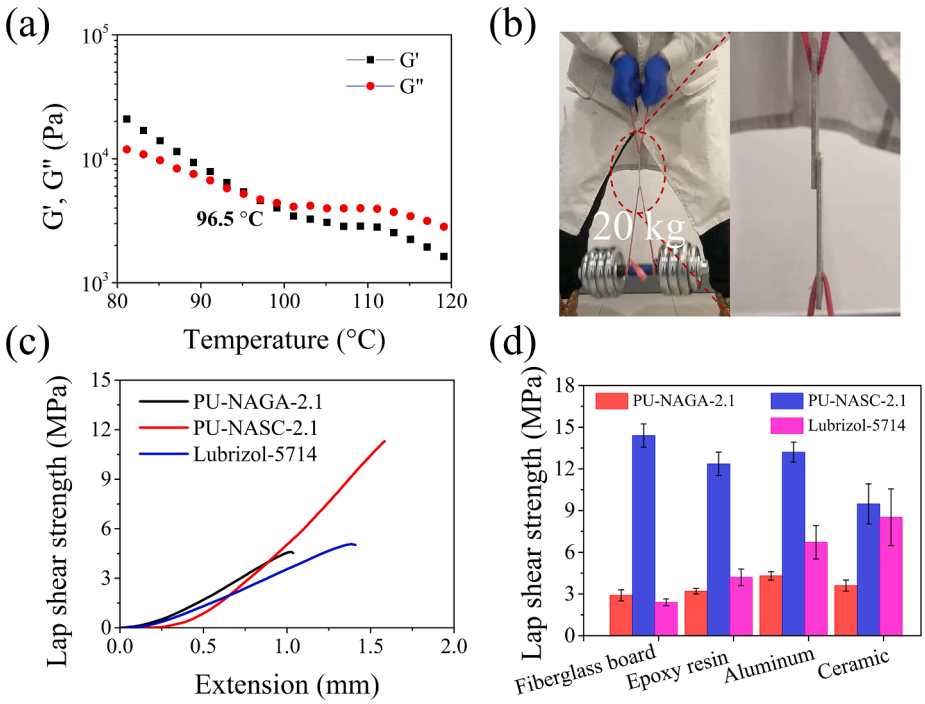

Fig. 4. Adhesive property of PU-NASC. a) Variation in the storage modulus and loss modulus as a function of temperature. b) Photograph showing that aluminum sheets bonded by PU-NASC-2.1 could lift a 20 kg dumbbell. c) Lap shear strength-extension curves of PU-NASC-2.1, PU-NAGA-2.1 and commercial adhesives bonded aluminum sheets. d) Lap shear strength of PU-NASC-2.1, PU-NAGA-2.1 and commercial adhesives in gluing various substrates.

curves of the PU-NASC-2.1, PU-NAGA-2.1 and representative commercial thermoplastic polyurethane adhesive Lubrizol 5714 in gluing aluminum sheets are shown in Fig. 4c. Clearly, the PU-NASC-2.1 displayed a much higher adhesion strength than PU-NAGA-2.1, and Lubrizol 5714 in bonding aluminum sheets, fiberglass board, epoxy resin, and ceramics, achieving 14.7 ± 0.8, 12.0 ± 0.7, 10.3 ± 0.7, 7.9 ± 1.2 MPa, respectively (Fig. 4d). An explanation for this is that the denser H-bonding interactions increased the cohesive energy of PU-NASC-2.1 and thus enhanced the adhesion strength.

3.4. 3D printing property of PU-NASC

The PU-NASC exhibited a transition from rubber state to viscous flow state under cyclic temperature sweep from 45 ℃ to 140 ℃ (Fig. 5a), in which no polymer degradation was detected by thermogravimetric analysis (Fig. S11). Thus, we further evaluated the 3D printing property of PU-NASC by melt extrusion technology. A series of PU-NASC-based architectures could be printed at an extruder barrel temperature of 140 °C, including a round grid, double-layered ring, meniscus of rabbit, and the pyramid of Khufu (Fig. 5g and Movie S3). The adjacent layers in the printed architectures were uniform and stable, indicating an excellent fidelity due to the strengthening effect of multiple H-bonds.

The printing resolution of the extruded filament could be controlled by various printing parameters such as the nozzle diameter, and raster width, which significantly affected the mechanical property of the final printed objects [37]. By regulating the printing parameters, an optimized filament diameter of 405 ± 11 μm was obtained according to the scanning electron microscope (SEM) image (Fig. S12). As observed in the SEM images, the surface pattern of printed filaments was relatively smooth, demonstrating a fluent printing behavior under the set printing temperature; while the cross-section pattern of the printed filaments was relatively rough, suggesting the ultrahigh toughness was resulted from multiple H-bonding interactions.

Next, we constructed rectangle grid specimens with varied raster width from 0.5 to 1.2 mm to verify the effect of raster width on the mechanical properties (Fig. 5b). The tensile strength and Young's modulus of the printed PU-NASC specimens were both decreased with the increase of raster width, achieving a tensile strength from 7.2 ± 1.6 MPa to 3.8 ± 0.2 MPa, and a Young's modulus from 141.6 ± 9.5 MPa to 51.9 ± 11.3 MPa (Fig. 5c ~ d). These results indicate that mechanical properties of printed objects could be adjusted by raster width to meet the requirement of the application. It is also noticed that the mechanical properties of the printed specimens were lower than those of the casting specimens owing to the existence of interspace in the printed structure. Nevertheless, the interspace in the printed structure could bring air in, thus improving the comfortability of the printed wearing device. In case of balancing the mechanical strength and air permeability, the raster width of the follow-up printing was set as 0.6 mm, and the corresponding tensile strength and Young's modulus were 6.1 ± 0.2 MPa and 98.5 ± 5.5 MPa, respectively.

Herein, a double-layered ring was printed, and the mechanical behavior was also evaluated via a compression test with different resting time. As shown in the force-strain curve in Fig. 5e, the curve nearly displayed a linear region up to a 50% strain, demonstrating an excellent elasticity. After 30 or 60-min resting period, the force-strain curves were nearly overlapped with the original one, indicating the excellent elastic recovery of double-layered ring. Moreover, the printed cylinder grid (diameter: 5 mm; thickness: 2.5 mm) showed a compressive modulus of

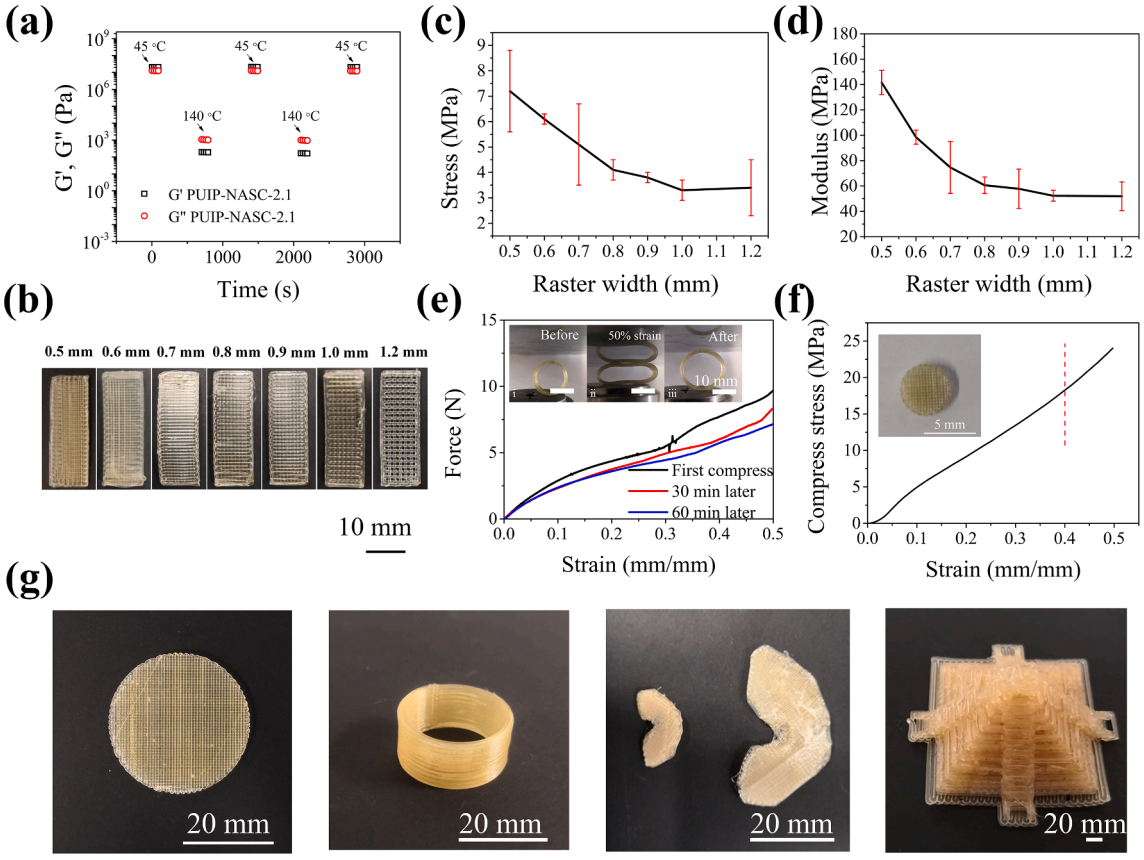

Fig. 5. 3D printing properties of PU-NASC. a) Cyclic temperature sweeps with the PU-NASC-2.1 inks being alternatively subjected to lower (45 °C, printing platform) and higher temperature (140 °C, printing nozzle) treatment. b) Digital images of 3D printed rectangle grids with raster width varying from 0.5 to 1.2 mm, and the corresponding c) tensile strength and d) Young's modulus. e) Compression behavior of 3D printed double-layer ring with different resting times. f) Compression behavior of the 3D printed disk grid. g) Digital images of 3D printed round grid, double-layered ring, meniscus, and pyramid objects.

50.4 ± 4.1 MPa and a compressive strength of 15.9 ± 2.1 MPa at a strain of 40% (Fig. 5f). The printed double-layer ring and the rectangle grid both could maintain structure stability without a noticeable deformation when a weight of 200 g was applied on it (Fig. S13 a ~ b and Movie S4). Intriguingly, the double-layer ring and the rectangle grid could bond together to construct a finger orthosis by holt-melting method (Fig. S13c).

3.5. 3D printing finger orthosis for monitoring key signs

Then, the finger orthosis with patient-specific geometry was printed using PU-NASC as an ink by melt extrusion 3D printing technology, which was based on a computer-aid design (CAD) model from seven parameters of a patient's index finger (Fig. S14) [3]. As shown in Fig. 6a, the orthosis model was designed with a constraint at the rear of the orthosis to maintain a full extension at the DIP joint, and an open ventilation section above the nail and several vents on the wall to allow for airflow and reduce sweating when it was worn. The 3D printed finger orthosis was worn on the index finger of a 27-year-old male volunteer, and could maintain the stability and full extension of the DIP joint, which was beneficial for recovery of the injured finger (Fig. 6b). Furthermore, the 3D printed orthosis could pass the X-ray, allowing for CT examination of a patient's injured finger joints (Fig. 6c).

In addition, a finite element analysis (FEA) that simulated the situation of pressed was conducted (Fig. 6d ~ e and Fig. S15). As presented in Fig. 6f, the maximum deflection and stress were decreased from orthosis to finger, indicating the sufficient protection of the mallet finger. Another simulation in a static structure module was conducted to estimate the required compressive strength of orthosis for keep full extension of the mallet finger. The rear of the orthosis was fixed, and the load applied at the front of the orthosis was calculated as 20.33 N. At the same time, the front area of the orthosis was squeezed, and the maximum deformation and compressive stress of orthosis were 0.8 mm (approximately 40% strain) and 11.2 MPa, respectively. The compressive stress at identical strain was 15.9 ± 2.1 MPa, higher than 11.2 MPa, suggesting that it could meet the requirement.

Due to the rich blood vessels in the fingertip, it is reliable to measure the vital signals like heart rate (HR) and peripheral capillary oxygen saturation (SpO_2) to assay the physiologic status of the patient [38]. Particularly, by recording the vital signals, we can better evaluate the recovery state of the mallet finger [39]. In consideration of the adhesiveness of PU-NASC, we attached a wireless pulse oximeter on the tip of the finger orthosis by hot-melting method to monitor the vital signals including the blood oxygen saturation, heart rate, blood pressure and pulse wave (Fig. 6g ~ h and Fig. S17) [40]. These signals are in the normal range, reflecting healthy state [18]. The recorded data could be transmitted via Bluetooth, and the strong adhesion could maintain stable contact between the fingertip and the oximeter, ensuring a reliable signal transmission (Fig. S18 and Movie S5).

Considering the on-skin wearing application of printed orthosis, the

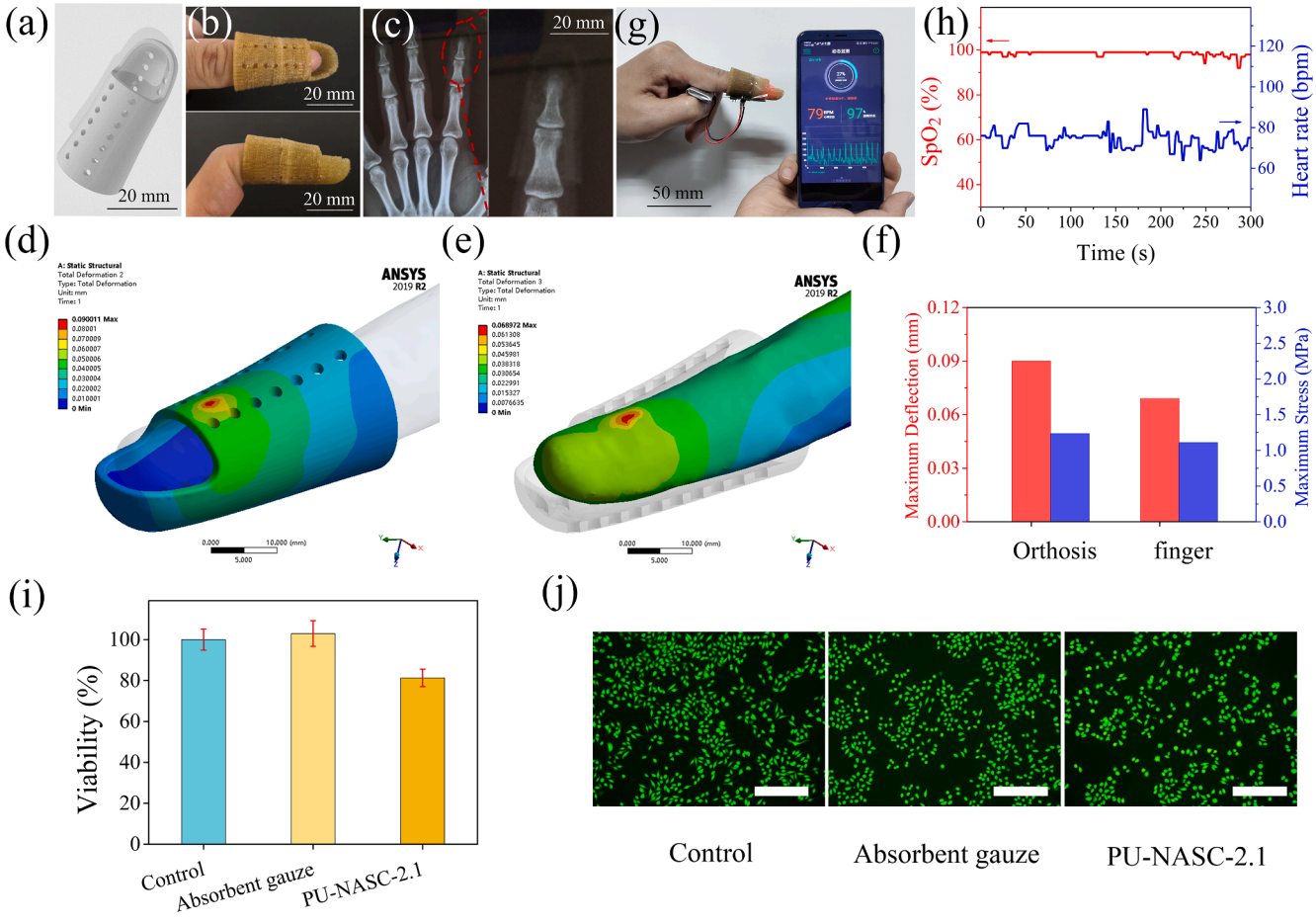

Fig. 6. 3D printing of finger orthosis for monitoring vital physiological signs. a) 3D model of the finger orthosis designed by CAD software. b) Top view (up) and front view (bottom) of the 3D printed orthosis worn on the index finger. c) X-ray transmittance photograph of the index finger wearing a 3D printing orthosis. d-e) Deflection simulation results of orthosis and finger under a load of 10 N. f) Comparison of the maximum deflection and stress between orthosis and finger. g) Attachment of a wireless pulse oximeter onto the orthosis by a hot-melt PU-NASC. h) Continuous recording of vital signals including saturated blood oxygen (SpO_2) and heart rate (HP). i) Cell viability and j) fluorescein staining image of fibroblast L-929 cells after 1 d co-cultivation with PU-NASC-2.1 extract liquid. Scale bar: 300 μm.

cytocompatibility of PU-NASC-2.1 was evaluated. The PU-NASC-2.1 exhibited low cytotoxicity by co-culturing fibroblast L-929 cells with its extracting liquid (Fig. 6i ~ j), indicating good cytocompatibility.

4. Conclusions

In summary, we fabricated a ultrastiff and tough polyurethane with a Young's modulus of 213.0 ± 3.7 MPa and toughness of 47.8 ± 1.9 MJ m^{-3}, based on a novel chain extender containing multiple H-bonds in the side chain. The PU-NASC exhibited an excellent adhesiveness in bonding various substrates and 3D printing ability at an elevated temperature resulting from dynamic H-bonding interactions. A series of PU-NASC based architectures with high fidelity could be printed. With an aim to treat mallet finger to fit the individual anthropometrics, we printed a PU-NASC-based orthosis, which could well fix the injured index finger of a volunteer. Thanks to the adhesiveness of PU-NASC, a commercial pulse oximeter was attached on the finger orthosis by hot-melting method to monitor the real-time vital physiological signs, which could be transmitted via Bluetooth. Thus, this stiff TPU is promising to develop a new medical external fixation scaffold to realize personalized therapy.

Declaration of Competing Interest

The authors declare that they have no known competing financial interests or personal relationships that could have appeared to influence the work reported in this paper.

Acknowledgments

The authors gratefully acknowledge the support for this work from National Key Research and Development Program (Grant No. 2018YFA0703100) and National Natural Science Foundation of China (Grant No. 51733006).

Appendix A. Supplementary data

Supplementary data to this article can be found online at https://doi.org/10.1016/j.cej.2021.133260.

References

[1] D.R. Ramponi, S.D. Hellier, Mallet finger, Adv. Emerg. Nurs. J. 41 (3) (2019) 198–203, https://doi.org/10.1097/TME.0000000000000251.
[2] S.R. Alla, N.D. Deal, I.J. Dempsey, Current concepts: mallet finger, Hand (N Y) 9 (2) (2014) 138–144, https://doi.org/10.1007/s11552-014-9609-y.
[3] A. Zolfagharian, T.M. Gregory, M. Bodaghi, S. Gharaie, P. Fay, Patient-specific 3D-printed splint for mallet finger injury, Int. J. Bioprint. 6 (2) (2020) 259, https://doi.org/10.18063/ijb.v6i2.259.
[4] G.P. Crawford, The molded polythene splint for mallet finger deformities, J. Hand. Surg. 9 (2) (1984) 231–237, https://doi.org/10.1016/s0363-5023(84)80148-3.
[5] S.V. Murphy, A. Atala, 3D bioprinting of tissues and organs, Nat. Biotechnol. 32 (8) (2014) 773–785, https://doi.org/10.1038/nbt.2958.
[6] Q. Ge, Z. Chen, J. Cheng, B. Zhang, Y.F. Zhang, H. Li, X. He, C. Yuan, J. Liu, S. Magdassi, S. Qu, 3D printing of highly stretchable hydrogel with diverse UV curable polymers, Sci. Adv. 7 (2) (2021), https://doi.org/10.1126/sciadv.aba4261.
[7] A. Valerga, M. Batista, J. Salguero, F. Girot, Influence of PLA filament conditions on characteristics of FDM parts, Materials 11 (8) (2018) 1322, https://doi.org/10.3390/ma11081322.
[8] H.S. Jang, S. Yoo, S.H. Kang, J. Park, G.-G. Kim, H.C. Ko, Automatic transformation of membrane-type electronic devices into complex 3D structures via extrusion shear printing and thermal relaxation of acrylonitrile-butadiene-styrene frameworks, Adv. Funct. Mater. 30 (5) (2020) 1907384, https://doi.org/10.1002/adfm.v30.510.1002/adfm.201907384.
[9] Q. Chen, J.D. Mangadlao, J. Wallat, A.l. De Leon, J.K. Pokorski, R.C. Advincula, 3D printing biocompatible polyurethane/poly(lactic acid)/graphene oxide nanocomposites: anisotropic properties, ACS Appl. Mater. Interfaces 9 (4) (2017) 4015–4023, https://doi.org/10.1021/acsami.6b1179310.1021/acsami.6b11793.s001.
[10] Y. Zhuo, Z. Xia, Y. Qi, T. Sumigawa, J. Wu, P. Šesták, Y. Lu, V. Håkonsen, T. Li, F. Wang, W. Chen, S. Xiao, R. Long, T. Kitamura, L. Li, J. He, Z. Zhang, Simultaneously toughening and stiffening elastomers with octuple hydrogen bonding, Adv. Mater. 33 (23) (2021) 2008523, https://doi.org/10.1002/adma.v33.2310.1002/adma.202008523.
[11] H. Zhang, Y. Chen, Y. Lin, X. Fang, Y. Xu, Y. Ruan, W. Weng, Spiropyran as a mechanochromic probe in dual cross-linked elastomers, Macromolecules 47 (19) (2014) 6783–6790, https://doi.org/10.1021/ma500760p.
[12] C.-Y. Shi, Q.i. Zhang, C.-Y. Yu, S.-J. Rao, S. Yang, H.e. Tian, D.-H. Qu, An ultrastrong and highly stretchable polyurethane elastomer enabled by a zipper-like ring-sliding effect, Adv. Mater. 32 (23) (2020) 2000345, https://doi.org/10.1002/adma.v32.2310.1002/adma.202000345.
[13] Y. Yao, Z. Xu, B.o. Liu, M. Xiao, J. Yang, W. Liu, Multiple H-bonding chain extender-based ultrastiff thermoplastic polyurethanes with autonomous self-healability, solvent-free adhesiveness, and AIE fluorescence, Adv. Funct. Mater. 31 (4) (2021) 2006944, https://doi.org/10.1002/adfm.v31.410.1002/adfm.202006944.
[14] Y. Eom, S.M. Kim, M. Lee, H. Jeon, J. Park, E.S. Lee, S.Y. Hwang, J. Park, D.X. Oh, Mechano-responsive hydrogen-bonding array of thermoplastic polyurethane elastomer captures both strength and self-healing, Nat. Commun. 12 (1) (2021) 621, https://doi.org/10.1038/s41467-021-20931-z.
[15] P. Song, H. Wang, High-performance polymeric materials through hydrogen-bond cross-linking, Adv. Mater. 32 (18) (2020) 1901244, https://doi.org/10.1002/adma.v32.1810.1002/adma.201901244.
[16] C. Fan, B. Liu, Z. Xu, C. Cui, T. Wu, Y. Yang, D. Zhang, M. Xiao, Z. Zhang, W. Liu, Polymerization of N-acryloylsemicarbazide: a facile and versatile strategy to tailor-make highly stiff and tough hydrogels, Mater. Horizons 7 (4) (2020) 1160–1170, https://doi.org/10.1039/c9mh01844a.
[17] H. Choi, A. Seo, J. Lee, Mallet finger lattice casts using 3D printing, J. Healthc. Eng. 2019 (2019) 1–5, https://doi.org/10.1155/2019/4765043.
[18] P.J. Chacon, L. Pu, T.H. da Costa, Y.-H. Shin, T. Ghomian, H. Shamkhalichenar, H.-C. Wu, B.A. Irving, J.-W. Choi, A wearable pulse oximeter with wireless communication and motion artifact tailoring for continuous use, IEEE Trans. Biomed. Eng. 66 (6) (2019) 1505–1513, https://doi.org/10.1109/TBME.1010.1109/TBME.2018.2874885.
[19] A.Y. Rwei, W. Lu, C. Wu, K. Human, E. Suen, D. Franklin, M. Fabiani, G. Gratton, Z. Xie, Y. Deng, S.S. Kwak, L. Li, C. Gu, A. Liu, C.M. Rand, T.M. Stewart, Y. Huang, D.E. Weese-Mayer, J.A. Rogers, A wireless, skin-interfaced biosensor for cerebral hemodynamic monitoring in pediatric care, Proc. Natl. Acad. Sci. U S A. 117 (50) (2020) 31674–31684, https://doi.org/10.1073/pnas.2019786117.
[20] K. Song, W. Ye, X. Gao, H. Fang, Y. Zhang, Q. Zhang, X. Li, S. Yang, H. Wei, Y. Ding, Synergy between dynamic covalent boronic ester and boron–nitrogen coordination: strategy for self-healing polyurethane elastomers at room temperature with unprecedented mechanical properties, Mater. Horizons 8 (1) (2021) 216–223, https://doi.org/10.1039/d0mh01142h.
[21] C. Cui, C. Fan, Y. Wu, M. Xiao, T. Wu, D. Zhang, X. Chen, B.o. Liu, Z. Xu, B.o. Qu, W. Liu, Water-Triggered hyperbranched polymer universal adhesives: from strong underwater adhesion to rapid sealing hemostasis, Adv. Mater. 31 (49) (2019) 1905761, https://doi.org/10.1002/adma.v31.4910.1002/adma.201905761.
[22] B.o. Liu, Z. Xu, H. Gao, C. Fan, G. Ma, D. Zhang, M. Xiao, B. Zhang, Y. Yang, C. Cui, T. Wu, X. Feng, W. Liu, Stiffness self-tuned shape memory hydrogels for embolization of aneurysms, Adv. Funct. Mater. 30 (22) (2020) 1910197, https://doi.org/10.1002/adfm.v30.2210.1002/adfm.201910197.
[23] S. Liang, Y. Zhang, H. Wang, Z. Xu, J. Chen, R. Bao, B. Tan, Y. Cui, G. Fan, W. Wang, W. Wang, W. Liu, Paintable and rapidly bondable conductive hydrogels as therapeutic cardiac patches, Adv. Mater. 30 (23) (2018) 1704235, https://doi.org/10.1002/adma.v30.2310.1002/adma.201704235.
[24] R.P. Chartoff, S. Rodrigues, M.L. Galaska, A.K. Sircar, Glass transition of elastomers using thermal analysis techniques, Rubber. Chem. Technol. 72 (3) (1999) 513–552, https://doi.org/10.5254/1.3538816.
[26] J. Li, M. Xiao, Y. Wang, J. Yang, W. Liu, Robust and antiswelling hollow hydrogel tube with antibacterial and antithrombotic ability for emergency vascular replacement, ACS Appl. Biol. Mater. 4 (4) (2021) 3598–3607, https://doi.org/10.1021/acsabm.1c0009610.1021/acsabm.1c00096.s00110.1021/acsabm.1c00096.s002.
[27] Q. Li, Z. Xu, D. Zhang, J. Yang, W. Liu, T-shaped trifunctional crosslinker-toughening hydrogels, Sci. China Technol. Sci. 63 (9) (2020) 1721–1729, https://doi.org/10.1007/s11431-020-1537-6.
[28] Y. Song, Y. Liu, T. Qi, G.L. Li, Towards dynamic but supertough healable polymers through biomimetic hierarchical hdrogen-bonding interactions, Angew. Chem. Int. Ed. 57 (42) (2018) 13838–13842, https://doi.org/10.1002/anie.201807622.
[29] J. Yu, K.e. Wang, C. Fan, X. Zhao, J. Gao, W. Jing, X. Zhang, J. Li, Y. Li, J. Yang, W. Liu, An ultrasoft self-fused supramolecular polymer hydrogel for completely preventing postoperative tissue adhesion, Adv. Mater. 33 (16) (2021) 2008395, https://doi.org/10.1002/adma.v33.1610.1002/adma.202008395.
[30] W. Kong, Y. Yang, Z. Liu, L. Jiang, C. Zhou, J. Lei, Structure-property relations of nylon-6 and polytetramethylene glycol based multiblock copolymers with microphase separation prepared through reactive processing, Polym. Int. 66 (3) (2017) 436–442, https://doi.org/10.1002/pi.2017.66.issue-310.1002/pi.5278.
[31] J. Hentschel, A.M. Kushner, J. Ziller, Z. Guan, Self-healing supramolecular block copolymers, Angew. Chem. Int. Ed. 51 (42) (2012) 10561–10565, https://doi.org/10.1002/anie.201204840.
[32] X. Wang, S. Zhan, Z. Lu, J. Li, X. Yang, Y. Qiao, Y. Men, J. Sun, Healable, recyclable, and mechanically tough polyurethane elastomers with exceptional damage tolerance, Adv. Mater. 32 (50) (2020) 2005759, https://doi.org/10.1002/adma.v32.5010.1002/adma.202005759.
[33] I.S. Jouibari, V. Haddadi-Asl, M.M. Mirhosseini, A novel investigation on micro-phase separation of thermoplastic polyurethanes: simulation, theoretical, and

experimental approaches, Iran. Polym. J. 28 (3) (2019) 237–250, https://doi.org/10.1007/s13726-019-00695-6.
[34] J. Kang, D. Son, G.-J. Wang, Y. Liu, J. Lopez, Y. Kim, J.Y. Oh, T. Katsumata, J. Mun, Y. Lee, L. Jin, J.-H. Tok, Z. Bao, Tough and water-Insensitive self-healing elastomer for robust electronic skin, Adv. Mater. 30 (13) (2018) 1706846, https://doi.org/10.1002/adma.v30.1310.1002/adma.201706846.
[35] Z. Xu, C. Fan, Q. Zhang, Y. Liu, C. Cui, B.o. Liu, T. Wu, X. Zhang, W. Liu, A self-thickening and self-strengthening strategy for 3D printing high-strength and antiswelling supramolecular polymer hydrogels as meniscus substitutes, Adv. Funct. Mater. 31 (18) (2021) 2100462, https://doi.org/10.1002/adfm.v31.1810.1002/adfm.202100462.
[36] D. Wang, JianHua Xu, JiaoYang Chen, P.o. Hu, Y. Wang, W. Jiang, JiaJun Fu, Transparent, mechanically strong, extremely tough, self-recoverable, healable supramolecular elastomers facilely fabricated via dynamic hard domains design for multifunctional applications, Adv. Funct. Mater. 30 (3) (2020) 1907109, https://doi.org/10.1002/adfm.v30.310.1002/adfm.201907109.
[37] Y. Guo, S. Chen, L. Sun, L. Yang, L. Zhang, J. Lou, Z. You, Degradable and fully recyclable dynamic thermoset elastomer for 3D-printed wearable electronics, Adv. Funct. Mater. 31 (9) (2021) 2009799, https://doi.org/10.1002/adfm.v31.910.1002/adfm.202009799.
[38] S. Abdollahi, E.J. Markvicka, C. Majidi, A.W. Feinberg, 3D printing silicone elastomer for patient-specific wearable pulse oximeter, Adv. Healthc. Mater. 9 (15) (2020) 1901735, https://doi.org/10.1002/adhm.v9.1510.1002/adhm.201901735.
[39] J. Zanker, G. Duque, Rapid geriatric assessment of hip fracture, Clin. Geriatr. Med. 33 (3) (2017) 369–382, https://doi.org/10.1016/j.cger.2017.03.003.
[40] Y. Ma, J. Choi, A. Hourlier-Fargette, Y. Xue, H.U. Chung, J.Y. Lee, X. Wang, Z. Xie, D. Kang, H. Wang, S. Han, S.K. Kang, Y. Kang, X. Yu, M.J. Slepian, M.S. Raj, J. B. Model, X. Feng, R. Ghaffari, J.A. Rogers, Y. Huang, Relation between blood pressure and pulse wave velocity for human arteries, Proc. Natl. Acad. Sci. U S A. 115 (44) (2018) 11144–11149, https://doi.org/10.1073/pnas.1814392115.